ORIGINAL PAPER

Synthesis of Spinel MnCo$_2$O$_4$ by Thermal Decomposition of Carbonates and Kinetics of Thermal Decomposition of Precursor

**Kaituo Wang · Xuehang Wu · Wenwei Wu ·
Yongmei Hu · Sen Liao**

Abstract The cubic MnCo$_2$O$_4$ was prepared by calcining MnCO$_3$-2CoCO$_3$·1.5H$_2$O above 600 °C in air. The precursor and its calcined products were characterized by thermogravimetry and differential scanning calorimetry, Fourier transform infrared spectroscopy, X-ray powder diffraction, scanning electron microscopy, and vibrating sample magnetometer. The result showed that high-crystallized MnCo$_2$O$_4$ with cubic structure [space group Fd-3m(227)] was obtained when the precursor was calcined above 600 °C in air for 6 h. Magnetic characterization indicated that cubic MnCo$_2$O$_4$ behaved weak magnetic behavior at room temperature. The thermal process of the precursor in air experienced three steps, which are: first, the dehydration of 1.5 water molecules, then the decomposition of MnCO$_3$-2CoCO$_3$ into cubic MnO$_2$ and cubic Co$_3$O$_4$, and at last the reaction of MnO$_2$ with Co$_3$O$_4$ into cubic MnCo$_2$O$_4$. Based on the KAS equation, the values of the activation energies associated with the thermal process of MnCO$_3$-2CoCO$_3$·1.5H$_2$O were determined.

Keywords MnCo$_2$O$_4$ · Chemical synthesis · Thermal decomposition · Non-isothermal kinetics

K. Wang · X. Wu · W. Wu (✉) · S. Liao
School of Chemistry and Chemical Engineering, Guangxi University, Nanning 530004, PR China
e-mail: gxuwuwenwei@aliyun.com

Y. Hu
Supervision and Inspection Station of Metallurgical Products Quality of Guangxi, Nanning 530023, PR China

1 Introduction

Spinel mixed oxides with general formula AB$_2$O$_4$ can be considered strategic materials due to their electronic, magnetic, optical, catalytic properties, and electrochemical properties [1–10]. These materials contain either alkaline earth metal and 3d transition metals or only 3d transition metals. MnCo$_2$O$_4$ is very important mixed oxides with inverted spinel structure, which can be depicted in the chemical formula Co^{2+}[Co^{2+}Mn^{4+}]O$_4$ [11]. From X-ray absorption measurements, it has been confirmed that a number of valence states exist in the spinels containing Co and Mn and that the mean charge of Mn ion in these compounds is close to 4$^+$ [12]. Compared with other spinel oxides, spinel MnCo$_2$O$_4$ has shown good catalytic activity for the oxygen reduction reaction in alkaline conditions [13]. Therefore, spinel MnCo$_2$O$_4$ is a promising candidate for the development of low-cost and practical electrically rechargeable metal–air batteries [14]. The quality of MnCo$_2$O$_4$ powders strongly depends on the synthesis method and conditions, which determine particle size, morphology, lattice parameters, stoichiometry, and average Mn valence of MnCo$_2$O$_4$ associated with catalytic and electrochemical performances [15, 16]. Preparations of high-quality samples with superfine particle size and/or doping have generally been considered to improve the catalytic and electrochemical performances of MnCo$_2$O$_4$.

To date, various methods of synthesizing spinel MnCo$_2$O$_4$ have been developed, including the Pechini method using a polymeric precursor [9], the refluxing method [10], the ceramic method [11], microwave synthesis [13], the hard template method [15], the sol-gel method [16], thermal decomposition of binary oxalates [12, 17], hydrothermal synthesis [18], the wet method [19], combustion reaction [20], and the polymeric precursors method [21]. The composi-

tion, morphology, and crystalline phases of $MnCo_2O_4$ associated with its properties are reportedly highly dependent on the starting materials, synthesis, and processing methods. For example, Liu and Yang [10] obtained cubic $MnCo_2O_4$ with nanospheres and stacked nanoplates morphology by a polyol-based precursor route using $Mn(CH_3COO)_2 \cdot 4H_2O$, $Co(CH_3COO)_2 \cdot 4H_2O$, and poly(vinyl-pyrrolidone) (PVP) as starting materials. The catalyst with spherical shape shows relatively higher activity than the plate for catalytic oxidation of CO to CO_2. Yoon et al. [20] synthesized single phase $MnCo_2O_4$ by the combustion reaction using H_2NCH_2COOH, $Mn(NO_3)_2 \cdot 6H_2O$, and $Co(NO_3)_2 \cdot 6H_2O$ as starting materials. Most researchers attempt to obtain single phase $MnCo_2O_4$ with high properties at the lowest possible cost. However, many $MnCo_2O_4$ synthesis methods are a complex process and have a high cost. Therefore, new synthesis methods for cubic $MnCo_2O_4$ are needed to be studied and innovated further. Besides, kinetics research of the thermal process of the $MnCo_2O_4$ precursor still has fewer reports in comparison with the synthesis of $MnCo_2O_4$.

This study aimed to prepare spinel $MnCo_2O_4$ by calcining $MnCO_3\text{-}2CoCO_3 \cdot 1.5H_2O$ obtained via a solid-state reaction at low heating temperatures and to study the kinetics of thermal decomposition of the precursor. The kinetics of thermal decomposition of the precursor was studied using TG/DSC techniques. Non-isothermal kinetics of thermal decomposition of the precursor was interpreted by the Kissinger–Akahira–Sunose (KAS) equation [22–27]. The kinetic parameters (E_a, A) and mechanisms of thermal decomposition of $MnCO_3\text{-}2CoCO_3 \cdot 1.5H_2O$ were discussed for the first time.

2 Experimental

2.1 Reagent and Apparatus

All chemicals were of reagent-grade purity (purity >99.9 %). Thermogravimetry and differential scanning calorimetry (TG/DSC) measurements were taken using a Netzsch Sta 409 PC/PG thermogravimetric analyzer under a continuous flow of air (40 mL min^{-1}) and sample mass was around 13 mg. X-ray powder diffraction (XRD) was performed using a Rigaku D/Max 2500V diffractometer equipped with a graphite monochromator and a Cu target. The radiation applied was Cu Kα ($\lambda = 0.15406$ nm), operated at 40 kV and 50 mA. XRD scans were made from 5° to 70° in 2θ with a step size of 0.02°. Fourier transform infrared (FT-IR) spectra of the precursor and its calcined products were recorded on a Nexus 470 FT-IR instrument. The morphologies of the synthesis products were observed using an S-3400 scanning electron microscope (SEM). The specific magnetization (M) of the calcined sample powders was carried out at room temperature using a vibrating sample magnetometer (Lake Shore 7410).

2.2 Preparation of $MnCo_2O_4$

The $MnCo_2O_4$ precursor was prepared by solid-state reaction at low heating temperatures [22, 23] using $MnSO_4 \cdot H_2O$, $CoSO_4 \cdot 7H_2O$, and $Na_2CO_3 \cdot 10H_2O$ as raw materials. In a typical synthesis, $MnSO_4 \cdot H_2O$ (19.16 g), $CoSO_4 \cdot 7H_2O$ (63.73 g), $Na_2CO_3 \cdot 10H_2O$ (71.38), and surfactant polyethylene glycol (PEG)-400 (4.0 mL, 50 vol.%) were placed in a mortar, and the mixture was thoroughly ground by hand with a rubbing mallet for 35 min. The grinding velocity was about 220 cycles/min, and the strength applied was moderate. The reactant mixture gradually became damp, and then a paste formed quickly. The reaction mixture was kept at room temperature for 1.5 h. The mixture was washed with deionized water to remove soluble inorganic salts until SO_4^{2-} ion could not be visually detected with a 0.5 mol L^{-1} BaCl$_2$ solution. The solid was then washed with a small amount of anhydrous ethanol and dried at 80 °C for 6 h. The resulting material was subsequently determined to be $MnCO_3\text{-}2CoCO_3 \cdot 1.5H_2O$. Cubic $MnCo_2O_4$ was obtained via calcining $MnCO_3\text{-}2CoCO_3 \cdot 1.5H_2O$ above 600 °C in air for 6 h.

3 Method of Determining Kinetic Parameters and Mechanism Functions

3.1 Determination of Activation Energy by the KAS Equation

Activation energy of thermal decomposition of the solid compound can be obtained by the KAS equation (Eq. (1)).

$$\ln \frac{q}{T^2} = \ln \frac{AR}{g(\alpha)E_a} - \frac{E_a}{RT} \tag{1}$$

where q is the heating rate (K min^{-1}), T is the reaction temperature (K) in TG curve, E_a is the activation energy (kJ mol^{-1}) of thermal decomposition, R is the gas constant (8.314×10^{-3} kJ mol^{-1} K^{-1}), A is the preexponential factor, and α is called the conversion degree.

The conversion degree (α) can be expressed as Eq. (2):

$$\alpha = \frac{m_i - m_t}{m_i - m_f} \tag{2}$$

where m_i, m_f and m_t are the initial, final, and current sample mass at the moment t, respectively. The $g(\alpha)$ is a function of α; it reveals the mechanism of reaction. The plot of $\ln(q/T^2)$ vs. $1/T$ corresponding to different values of α can be obtained by a linear regression of least-square method, respectively. Thus, reaction activation energy E_a can be obtained from linear slope ($-E_a/R$, Eq. (1)).
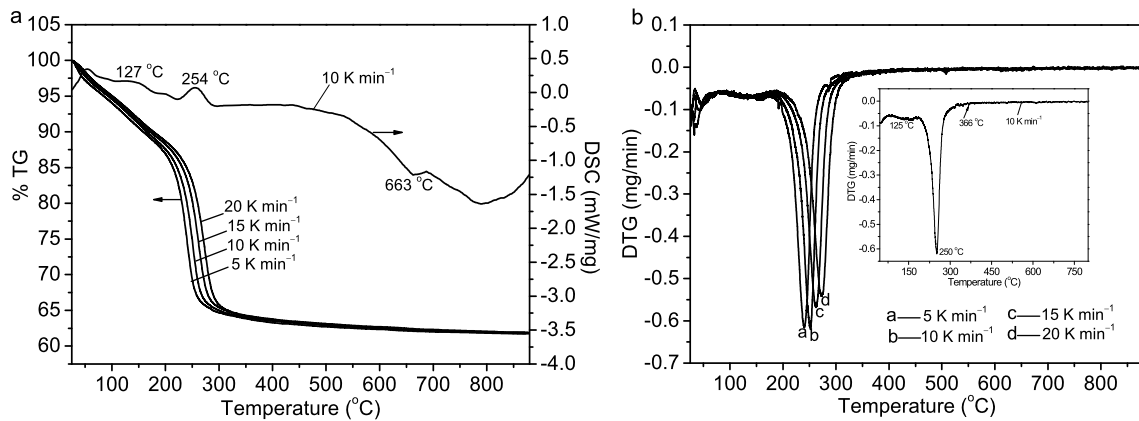
Fig. 1 TG/DTG/DSC curves of $MnCO_3$-$2CoCO_3 \cdot 1.5H_2O$ at different heating rates in air

3.2 Determination of Most Probable Mechanism Functions

The following equation was used to estimate the most probable reaction mechanism of thermal decomposition of $MnCO_3$-$2CoCO_3 \cdot 1.5H_2O$, i.e., $g(\alpha)$ function [23, 28]:

$$\ln g(\alpha) = \left[\ln \frac{AE_a}{R} + \ln \frac{e^{-x}}{x^2} + \ln h(x) \right] - \ln \beta, \qquad (3)$$

where $x = E_a/(RT)$, $h(x) = \frac{x^4+18x^3+86x^2+96x}{x^4+20x^3+120x^2+240x+120}$, and β is the heating rate ($K \min^{-1}$). The conversions α corresponding to multiple rates at the same temperature are put into the left of Eq. (3), combined with 31 types of mechanism functions [29–31], the slope k and correlation coefficient r^2 are obtained from the plot of $\ln g(\alpha)$ vs. $\ln \beta$. The probable mechanism function is the one for which the value of the slope k is near -1.00000 and correlation coefficient r^2 is better.

3.3 Calculation of Preexponential Factor A

The preexponential factor was estimated from Eq. (4) [32]:

$$A = \frac{\beta g(\alpha) E_\alpha}{RT_{\max}^2} \exp\left(\frac{E_\alpha}{RT_{\max}} \right) \qquad (4)$$

where A is the preexponential factor (s^{-1}), β is the heating rate ($K \min^{-1}$), $g(\alpha)$ is the most probable mechanism function determined by Eq. (3), E_α is the activation energy ($kJ \, mol^{-1}$) of thermal decomposition, R is the gas constant ($8.314 \times 10^{-3} \, kJ \, mol^{-1} \, K^{-1}$), and $T_{\max}$ is the most rapid decomposition temperature (i.e., peak temperature in differential thermogravimetry (DTG) curve, K).

4 Results and Discussion

4.1 TG/DTG/DSC Analysis of the Precursor

Figure 1 shows the TG/DTG/DSC curves of the precursor at four different heating rates in air from ambient temperature to 900 °C. The TG/DTG/DSC curves show that thermal decomposition of $MnCO_3$-$2CoCO_3 \cdot 1.5H_2O$ below 900 °C occurs in three well-defined steps. For a heating rate of 10 K min^{-1}, the first step starts at 20 °C, ends at 126 °C, and is characterized by a weak DTG peak at about 125 °C and a broad and weak endothermic DSC peak at 127 °C, which can be attributed to dehydration of one and a half water molecules from $MnCO_3$-$2CoCO_3 \cdot 1.5H_2O$ (mass loss: observed, 7.15 %; theoretical, 7.11 %). The second decomposition step starts at 126 °C, ends at 306 °C, and is characterized by a strong DTG peak at 250 °C and a stronger DSC endothermic peak at 254 °C, attributed to reaction of $MnCO_3$-$2CoCO_3$ with $5/6O_2$ into MnO_2, Co_3O_4, and of three CO_2 molecules (mass loss: observed, 27.35 %; theoretical, 27.74 %). The third decomposition step starts at 306 °C, ends at 600 °C, and is characterized by a weak DTG peak at 366 °C, attributed to reaction of MnO_2 with Co_3O_4 into $MnCo_2O_4$, and of $1/3O_2$ (mass loss: observed, 2.82 %; theoretical, 2.81 %). From Fig. 1a, the exothermic DSC peak at about 663 °C was ascribed to crystallization of cubic $MnCo_2O_4$.

4.2 IR Spectroscopic Analysis of the Precursor and Its Calcined Samples

The FT-IR spectra of the precursor and its calcined sample are shown in Fig. 2. The precursor exhibited a strong and broad band at about 3431 cm^{-1} that can be assigned to symmetric and asymmetric stretching modes of water molecules [33–36]. The strong band at 1453 cm^{-1} was at-

tributed to ν_3 mode of carbonate, and the band at 828 cm^{-1} were assigned to ν_2 mode of carbonate [37–39]. The band at 2340 cm^{-1} should be assigned to the asymmetric stretching of CO_2 (g), which was attributed to the sample adsorbing CO_2 from air [37, 40]. FT-IR spectra of the precursor and sample obtained at 150 °C are similar. Besides, FT-IR spectra of two samples obtained at 250 °C and 450 °C are similar. However, the FT-IR spectrum of the sample obtained at 600 °C has a little difference in comparison with those of the samples obtained at 250 °C and 450 °C. Such as, the bands at about 3431, 2027, 1638, and 1536 cm^{-1} became weak and/or disappeared, which implied that structure and composition of sample obtained at 600 °C has great difference in comparison with those of samples obtained at 250 °C and 450 °C. The spectrum of the calcined sample at 600 °C was in agreement with that of cubic $MnCo_2O_4$ from literature [16].
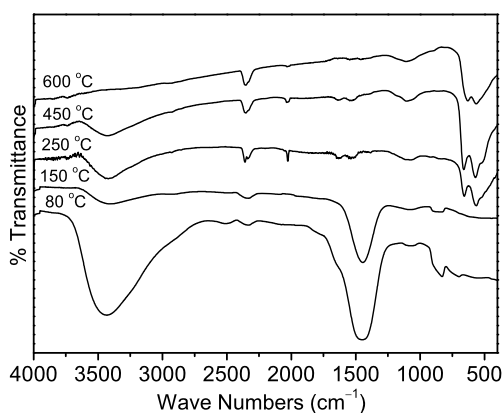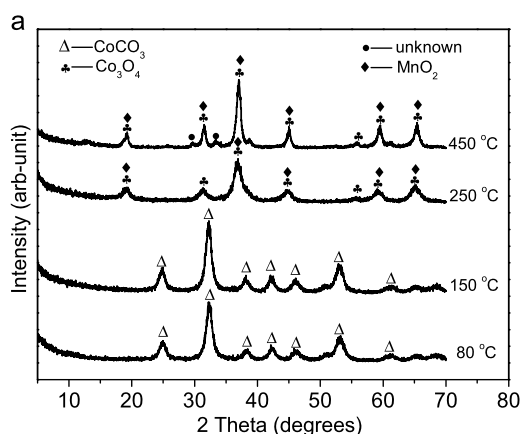

Fig. 2 FT-IR spectra of $MnCO_3$-$2CoCO_3 \cdot 1.5H_2O$ and its calcined samples

4.3 XRD Analysis of the Precursor and Its Calcined Samples

Figure 3 shows the XRD patterns of the precursor and its calcined samples. From Fig. 2a, the results showed that the precursor was a mixture containing rhombohedral $CoCO_3$ [PDF card 11-0692, space group R-3c(167)] and amorphous $MnCO_3$. The structure of the rhombohedral $CoCO_3$ is still stable up to 150 °C. When the precursor was calcined at 250 °C and 450 °C for 6 h, the characteristic diffraction peaks of cubic MnO_2 and Co_3O_4 appeared. However, when the precursor was calcined at 600 °C, strong intensity and smoothed baseline, and a wide and low diffraction pattern of the thermal decomposition product was observed. Except a weak diffraction peak of unknown compound, and three very weak diffraction peaks of MnO_2 and/or Co_3O_4, which were located at 15.8, 37.0, 59.5, and 65.2° for 2θ, respectively, were observed; all other the diffraction peaks in the pattern of sample obtained at 600 °C were in agreement with those of cubic $MnCo_2O_4$, with space group Fd-3m(227) and the following cell parameters: a = b = c = 0.8269 nm, $\alpha = \beta = \gamma = 90°$, density = 5.564 g cm^{-3}, from PDF card 23-1237, which indicated that the sample obtained at 600 °C was cubic $MnCo_2O_4$.

According to the Scherrer formula [22, 23]: $D = K\lambda / (\beta \cos \theta)$, where D is crystallite diameter, $K = 0.89$ (the Scherrer constant), $\lambda = 0.15406$ nm (wavelength of the X-ray used), β is the width of line at the half-maximum intensity, and θ is the corresponding angle. The resulting crystallite sizes of the products from the calcined precursor at 600, 700, and 850 °C in air for 6 h were 17.7, 27.8, and 47.9 nm, respectively. The crystallinity of cubic $MnCo_2O_4$ can be calculated via MDI Jade 5.0 software; the results showed that crystallinity of cubic $MnCo_2O_4$ obtained at 600, 700, and 850 °C were 78.15, 91.79, and 91.81 %, respectively.

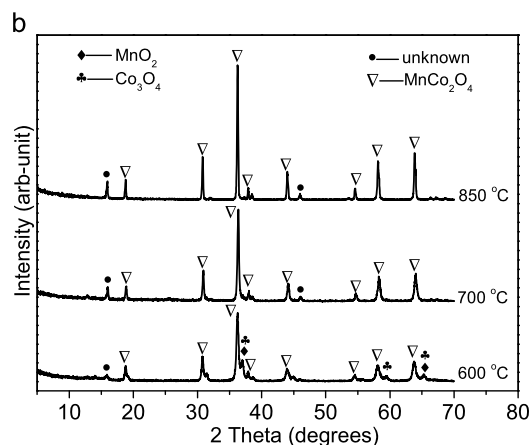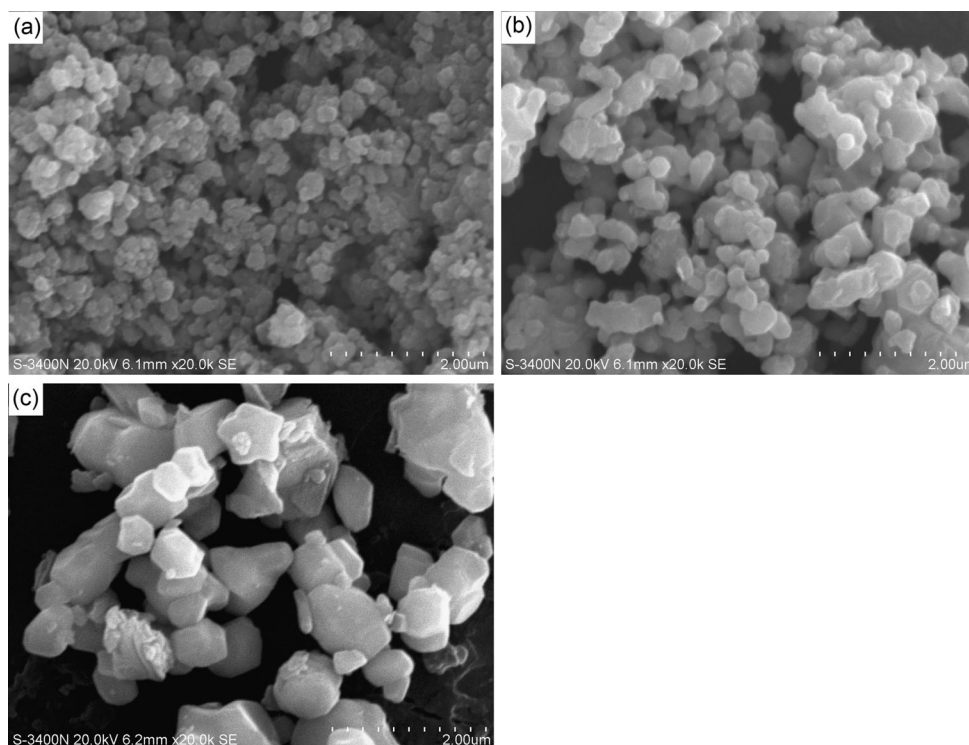**Fig. 3** XRD patterns of $MnCO_3$-$2CoCO_3 \cdot 1.5H_2O$ and its calcined samples at different temperatures for 6 h

Fig. 4 SEM micrographs of the products synthesized at different temperatures for 6 h: (**a**) 600 °C; (**b**) 700 °C; (**c**) 850 °C

4.4 SEM Analyses of the Calcined Samples

The morphologies of the calcined samples are shown in Fig. 4. From Fig. 4a, it can be seen that the calcined sample obtained at 600 °C was composed of approximately spherical grains; there is a soft agglomeration phenomenon among the particles of $MnCo_2O_4$, and the observed particles sizes are between 50 and 100 nm. With the increase of the calcination temperature, the crystallite in calcined sample was aggregated into larger grains further. Figure 4b and c show the SEM micrographs of samples obtained at 700 and 850 °C, respectively. The calcined sample at 700 °C still kept approximately spherical morphology, and particles sizes are mainly between 100 and 300 nm. However, the calcined sample obtained at 850 °C became polyhedral grains with a particle size of between 300 and 600 nm. The average crystallite sizes of the calcined samples determined by XRD were significantly smaller than the values determined by SEM. This can be attributed to that the values observed by the SEM technique gave the size of the secondary particles, which were composed of several or many crystallites by soft reunion, and the X-ray line broadening analysis disclosed only the size of single crystallite.
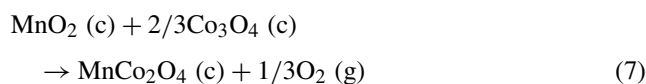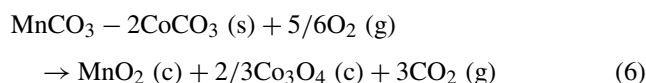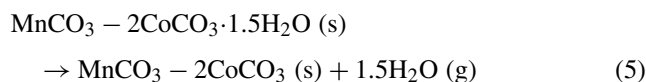
4.5 Magnetic Properties of the Calcined Samples

The magnetic properties of the calcined samples obtained at different temperatures are shown in Fig. 5. It can be observed that three samples exhibited weak magnetic behaviors at room temperature, and the specific magnetization of powders increased with the increase of the applied field. The specific magnetizations of the powders obtained at 600, 700, and 850 °C were 1.16, 0.83, and 0.72 emu g^{-1} under an applied field of 19.5 kOe, respectively. That is, the larger the crystallinity of cubic $MnCo_2O_4$, the smaller is the specific magnetization. Compared with other methods [9], specific magnetization of cubic $MnCo_2O_4$ obtained at 700 °C in this paper has little difference with that from other synthesis methods. For instance, Borges et al. [9] obtained spinel $MnCo_2O_4$ with nearly spherical morphology by the Pechini method. The results showed that the sample obtained at 700 °C had a specific magnetization of about 1.00 emu g^{-1} under an applied field of 1 T and a measure temperature of 120 K.

4.6 Kinetics of Thermal Decomposition of the Precursor

In accordance with TG/DTG/DSC, IR, and XRD analyses of the precursor and its calcined products mentioned above, thermal decomposition of the precursor below 900 °C consists of three steps, which can be expressed as follows:
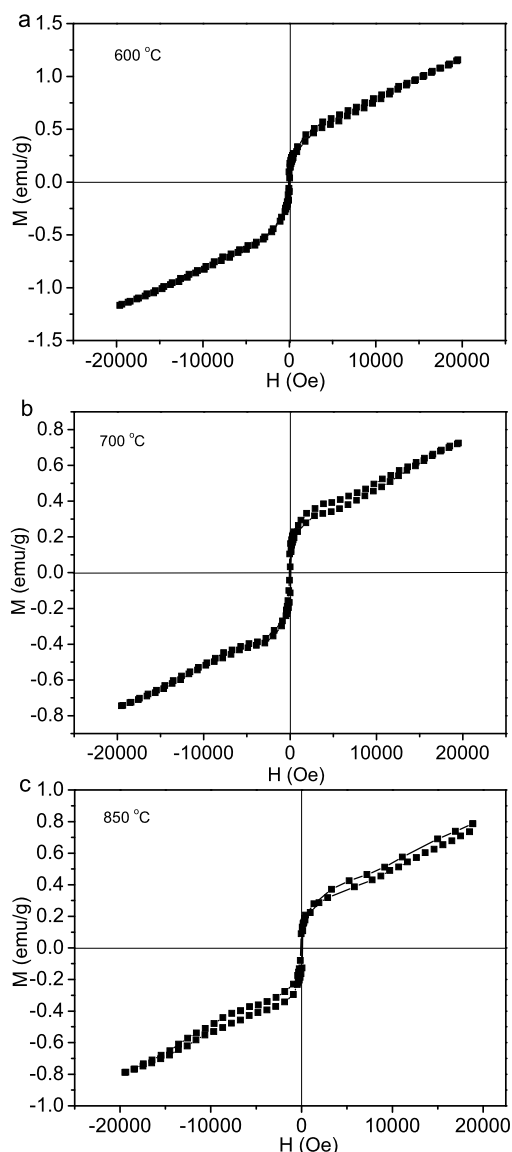
$$MnCO_3 - 2CoCO_3 \cdot 1.5H_2O \text{ (s)}$$
$$\rightarrow MnCO_3 - 2CoCO_3 \text{ (s)} + 1.5H_2O \text{ (g)} \qquad (5)$$

$$MnCO_3 - 2CoCO_3 \text{ (s)} + 5/6O_2 \text{ (g)}$$
$$\rightarrow MnO_2 \text{ (c)} + 2/3Co_3O_4 \text{ (c)} + 3CO_2 \text{ (g)} \qquad (6)$$

$$MnO_2 \text{ (c)} + 2/3Co_3O_4 \text{ (c)}$$
$$\rightarrow MnCo_2O_4 \text{ (c)} + 1/3O_2 \text{ (g)} \qquad (7)$$

Fig. 5 The specific magnetization (M) as a function of field (H) of calcined samples at different temperatures in air for 6 h

Fig. 6 The dependence of E_a on α at different thermal decomposition steps
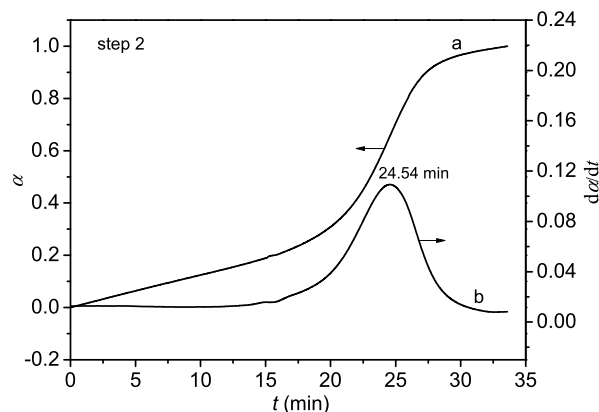
Fig. 7 Curves of α vs. t and $d\alpha/dt$ vs. t at heating rate of 5 K min^{-1}

According to the non-isothermal method, the basic data of α and T collected from the TG curves of thermal decomposition of MnCO$_3$-2CoCO$_3$·1.5H$_2$O at four heating rates (5, 10, 15, and 20 K min^{-1}). According to Eq. (1), the isoconversional calculation procedure of the KAS equation was used. The corresponding KAS lines for different decomposition steps were obtained at different conversion degrees α and different heating rates β at first, and then reaction activation energy E_a can be obtained from linear slope ($-E_a/R$). The results are shown in Fig. 6. From Fig. 6, the average values of the activation energies associated with thermal decomposition of MnCO$_3$-2CoCO$_3$·1.5H$_2$O were 88.24 ± 13.61 for step 1, 96.36 ± 7.12 for step 2, and 101.27 ± 35.14 kJ mol^{-1} for step 3, respectively. The activation energy changes in steps 1 and 3 with α are higher
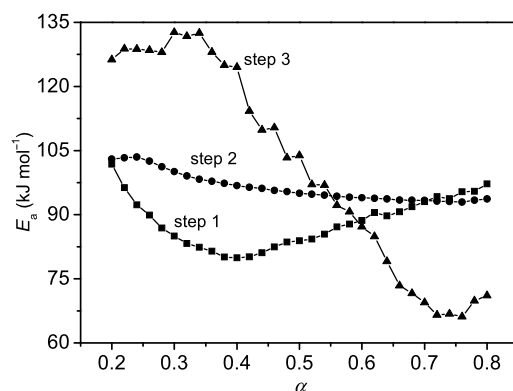
than 10 %, and those in step 2 with α are lower than 10 %, so that we draw a conclusion that dehydration of 1.5 water molecules from MnCO$_3$-2CoCO$_3$·1.5H$_2$O (step 1) and the reaction of MnO$_2$ with Co$_3$O$_4$ into MnCo$_2$O$_4$ (step 3) could be multi-step reaction mechanisms; the reaction of MnCO$_3$-2CoCO$_3$ with 5/6O$_2$ into MnO$_2$ and Co$_3$O$_4$ (step 2) is simple reaction mechanisms [28, 41–43]. The activation energy of steps 2 and 3 is higher than that of step 1, which implies that the steps 2 and 3 of thermal decomposition of MnCO$_3$-2CoCO$_3$·1.5H$_2$O may be interpreted as "slow" stages, while step 1 may be interpreted as a "fast" stage.

Figure 7 shows the curves of α vs. t and $d\alpha/dt$ vs. t for step 2. From Fig. 7a, step 2 is sigmoidal model (sometimes also called autocatalytic) [32, 43], which represents the process of step 2 whose initial and final stages demonstrate the accelerating and decelerating behavior, respectively, so that the process rate reaches its maximum at some values of the extent of conversion. The result shows that rate for step 2 reaches its maximum at 24.54 min (Fig. 7b).

We randomly choose several temperatures which corresponding conversions $0.10 < \alpha < 0.90$ at first, then conversions corresponding to an appropriate temperature for $\beta = 5$, 10, 15, and 20 K min^{-1} were put into thirty-one
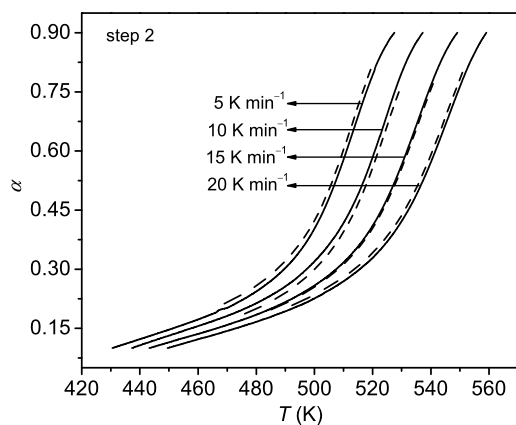
Fig. 8 Comparison of model results (*dash line*) with the experimental data (*solid line*) of the thermal decomposition of MnCO$_3$-2CoCO$_3$·1.5H$_2$O for step 2 at different heating rates

types of mechanism functions [29–31]. The slope k, correlation coefficient r^2, and intercept B of linear regression of ln $g(\alpha)$ vs. ln β were obtained. The two mechanism functions of better correlation coefficient r^2 were determined to be probable mechanism functions at first, and then several temperatures were randomly chosen to calculate the slope k, correlation coefficient r^2, and intercept B of the two probable mechanism functions by the same method. Mechanism function in which the value of k is the closest to -1.00000 and the correlation coefficient r^2 is higher is chosen as mechanism function of thermal decomposition of MnCO$_3$-2CoCO$_3$·1.5H$_2$O. The results showed that probable mechanism function integral form of thermal decomposition of MnCO$_3$-2CoCO$_3$·1.5H$_2$O for step 2 was determined to be $g(\alpha) = [1 - (1 - \alpha)^{1/3}]^2$. Rate-determining mechanism for step 2 is three-dimensional diffusion.

The preexponential factor was obtained from Eq. (4), inserting the most probable mechanism function $g(\alpha)$, β, E_a, R, and $T_{\max}$ values. The results showed that the preexponential factor of thermal decomposition of MnCO$_3$-2CoCO$_3$·1.5H$_2$O for step 2 was determined to be $A = 2.30 \times 10^7$ s^{-1}.

In order to prove the validity of the kinetic mechanisms for step 2 of thermal decomposition of MnCO$_3$-2CoCO$_3$·1.5H$_2$O, the comparisons were drawn between experimental data and results of the kinetic mechanism for every heating rate. The results are shown in Fig. 8. It can be found that the model-predicted plots were in agreement with the experimental plots, indicating that the mechanism function for step 2 of thermal decomposition of MnCO$_3$-2CoCO$_3$·1.5H$_2$O is reliable.

5 Conclusions

We have successfully synthesized cubic MnCo$_2$O$_4$ via thermal decomposition of binary carbonates. XRD analysis sug-

gested that high-crystallized MnCo$_2$O$_4$ with cubic structure was obtained when MnCO$_3$-2CoCO$_3$·1.5H$_2$O was calcined above 600 °C in air for 6 h. The crystallite size of MnCo$_2$O$_4$ synthesized at 600 °C for 6 h was about 18 nm. Magnetic characterization indicated that cubic MnCo$_2$O$_4$ sample exhibited a weak magnetic behavior at room temperature. The thermal decomposition of the precursor in air experienced three steps, which are: first, the dehydration of 1.5 water molecules, then the decomposition of MnCO$_3$-2CoCO$_3$ into MnO$_2$ and Co$_3$O$_4$, and at last the reaction of MnO$_2$ and Co$_3$O$_4$ into cubic MnCo$_2$O$_4$. The values of the activation energies associated with thermal decomposition of MnCO$_3$-2CoCO$_3$·1.5H$_2$O were determined to be 88.24 ± 13.61, 96.36 ± 7.12, and 101.27 ± 35.14 kJ mol^{-1} for the first, second, and third thermal decomposition steps, respectively. Thermal decomposition of MnCO$_3$-2CoCO$_3$·1.5H$_2$O for steps 1 and 3 could be multistep reaction mechanisms; reaction of MnO$_2$ with Co$_3$O$_4$ into MnCo$_2$O$_4$ is simple reaction mechanisms (step 2).

References

1. Maqsood, A., Faraz, A.: J. Supercond. Nov. Magn. **25**, 1025–1033 (2012)
2. Msomi, J.Z., Moyo, T., Abdallah, H.M.I.: J. Supercond. Nov. Magn. **25**, 2643–2646 (2012)
3. Wu, X.H., Wu, W.W., Zhou, K.W., Cui, X.M., Liao, S.: J. Therm. Anal. Calorim. **110**, 781–787 (2012)
4. Song, Q., Zhang, Z.J.: J. Am. Chem. Soc. **126**, 6164–6168 (2004)
5. Pankhurst, Q.A., Pollard, R.J.: J. Phys. Condens. Matter **5**, 8487–8508 (1993)
6. Abdallah, H.M.I., Moyo, T., Msomi, J.Z.: J. Supercond. Nov. Magn. **24**, 669–673 (2011)
7. Gong, C., Bai, Y.J., Qi, Y.X., Lun, N., Feng, J.: Electrochim. Acta **90**, 119–127 (2013)
8. Courtel, F.M., Abu-Lebdeh, Y., Davidson, I.J.: Electrochim. Acta **71**, 123–127 (2012)
9. Borges, F.M.M., Melo, D.M.A., Câmara, M.S.A., Martinelli, A.E., Soares, J.M., de Araújo, J.H., Cabral, F.A.O.: J. Magn. Magn. Mater. **302**, 273–277 (2006)
10. Liu, L., Yang, Y.Z.: Superlattices Microstruct. **54**, 26–38 (2013)
11. Joy, P.A., Date, S.K.: J. Magn. Magn. Mater. **210**, 31–34 (2000)
12. Bazuev, G.V., Korolyov, A.V.: J. Magn. Magn. Mater. **320**, 2262–2268 (2008)
13. Nissinen, T., Valo, T., Gasik, M., Rantanen, J., Lampinen, M.: J. Power Sources **106**, 109–115 (2002)
14. Koninck, M.D., Marsan, B.: Electrochim. Acta **53**, 7012–7021 (2008)
15. Zhu, J.K., Gao, Q.M.: Microporous Mesoporous Mater. **124**, 144–152 (2009)
16. Lavela, P., Tirado, J.L., Vidal-Abarca, C.: Electrochim. Acta **52**, 7986–7995 (2007)
17. Gyrdasova, O.I., Bazuev, G.V., Grigorov, I.G., Koryakova, O.V.: Inorg. Mater. **42**, 1126–1132 (2006)
18. Liu, H.W., Wang, J.: J. Electron. Mater. **41**, 3107–3110 (2012)

19. Yamamoto, N., Higashi, S., Kawano, S., Achiwa, N.: J. Mater. Sci. Lett. **2**, 525–526 (1983)
20. Yoon, M.Y., Lee, E.J., Song, R.H., Hwang, H.J.: Met. Mater. Int. **17**, 1039–1043 (2011)
21. dos Santos, M.E., Ferreira, R.A., Lisboa-Filho, P.N., Peña, O.: J. Magn. Magn. Mater. **329**, 53–58 (2013)
22. Wu, X.H., Zhou, K.W., Wu, W.W., Cui, X.M., Li, Y.N.: J. Therm. Anal. Calorim. **111**, 9–16 (2013)
23. Wu, W.W., Li, Y.N., Zhou, K.W., Wu, X.H., Liao, S., Wang, Q.: J. Therm. Anal. Calorim. **110**, 1143–1151 (2012)
24. Chrissafis, K.: J. Therm. Anal. Calorim. **95**, 273–283 (2009)
25. Wu, X.H., Wu, W.W., Zhou, K.W., Qin, L.Q., Liao, S., Lin, Y.J.: J. Supercond. Nov. Magn. (2013). doi:10.1007/s10948-013-2297-y
26. Wu, W.W., Cai, J.C., Wu, X.H., Wang, K.T., Hu, Y.M., Wang, Q.: J. Supercond. Nov. Magn. (2013). doi:10.1007/s10948-013-2227-z
27. Boonchom, B., Vittayakorn, N.: J. Chem. Eng. Data **55**, 3307–3311 (2010)
28. Zhou, K.W., Wu, W.W., Li, Y.N., Wu, X.H., Liao, S.: J. Therm. Anal. Calorim. **114**, 205–212 (2013)
29. Vlaev, L., Nedelchev, N., Gyurova, K., Zagorcheva, M.: J. Anal. Appl. Pyrolysis **81**, 253–262 (2008)
30. Liqing, L., Donghua, C.: J. Therm. Anal. Calorim. **78**, 283–293 (2004)
31. Jiang, H.Y., Wang, J.G., Wu, S.Q., Wang, B.S., Wang, Z.Z.: Carbon **48**, 352–358 (2010)
32. Vyazovkin, S., Burnham, A.K., Criado, J.M., Pérez-Maqueda, L.A., Popescu, C., Sbirrazzuoli, N.: Thermochim. Acta **520**, 1–19 (2011)
33. Wu, W.W., Cai, J.C., Wu, X.H., Liao, S., Huang, A.G.: Powder Technol. **215–216**, 200–205 (2012)
34. Li, Y.N., Wu, X.H., Wu, W.W., Wang, K.T., Liao, S.: J. Supercond. Nov. Magn. **26**, 2153–2158 (2013)
35. Huang, J.W., Su, P., Wu, W.W., Li, Y.N., Wu, X.H., Liao, S.: J. Supercond. Nov. Magn. **25**, 1971–1977 (2012)
36. Wu, W.W., Cai, J.C., Wu, X.H., Liao, S., Wang, K.T., Tao, L.: Adv. Powder Technol. **24**, 154–159 (2013)
37. Zhou, K.W., Wu, X.H., Wu, W.W., Xie, J., Tang, S.Q., Liao, S.: Adv. Powder Technol. **24**, 359–363 (2013)
38. Chandradass, J., Bae, D.S., Kim, K.H.: Adv. Powder Technol. **22**, 370–374 (2011)
39. Wu, X.H., Wu, W.W., Cui, X.M., Liao, S.: J. Therm. Anal. Calorim. **107**, 625–632 (2012)
40. Wu, X.H., Wu, W.W., Cui, X.M., Liao, S.: J. Therm. Anal. Calorim. **109**, 163–169 (2011)
41. Budrugeac, P., Muşat, V., Segal, E.: J. Therm. Anal. Calorim. **88**, 699–702 (2007)
42. Chaiyo, N., Muanghlua, R., Niemcharoen, S., Boonchom, B., Seeharaj, P., Vittayakorn, N.: J. Therm. Anal. Calorim. **107**, 1023–1029 (2012)
43. Wu, W.W., Wang, K.T., Li, Y.N., Wu, X.H., Liao, S., Wang, Q.: J. Therm. Anal. Calorim. **112**, 1391–1399 (2013)